



## Barotropic tides beneath the Amery Ice Shelf

M. A. Hemer,<sup>1,2</sup> J. R. Hunter,<sup>3</sup> and R. Coleman<sup>4</sup>

Received 4 April 2006; revised 20 June 2006; accepted 13 July 2006; published 14 November 2006.

[1] A barotropic tidal model has been applied to the Amery Ice Shelf cavity and Prydz Bay region of East Antarctica. The sensitivity of the tidal solution of the model to variation of the water column thickness of the Amery Ice Shelf cavity has been determined. A best estimate water column thickness grid is presented which both fits available water column thickness data (bed elevation and ice thickness) and results in reasonable agreement with available tidal elevation data. This is an important result for the Amery Ice Shelf given the severe lack of sub-ice shelf bed elevation and limited direct ice thickness measurements. Using the resulting topography, simulated tidal current speeds in the sub-Amery Ice Shelf cavity are significantly less than those beneath other major embayed Antarctic ice shelves, with maximum tidal current speeds of  $26 \text{ cm s}^{-1}$  indicated for this cavity. Similarly, the estimated energy dissipation beneath the Amery Ice Shelf due to surface friction of 6 MW is low in comparison with the other ice shelves. Tidally induced vertical mixing is found to be too weak to destroy the stratification associated with the relatively warm water in the lower part of the cavity and ice shelf meltwater in the upper part of the cavity. However, it is proposed that buoyancy-driven upwelling, rather than vertical mixing, is sufficient to bring the lower water mass into contact with the ice shelf. The depth-averaged model suggests that barotropic tidal processes have little influence on the oceanographic properties of the Amery Ice Shelf cavity.

**Citation:** Hemer, M. A., J. R. Hunter, and R. Coleman (2006), Barotropic tides beneath the Amery Ice Shelf, *J. Geophys. Res.*, *111*, C11008, doi:10.1029/2006JC003622.

### 1. Introduction

[2] The Amery Ice Shelf (hereafter AIS) is one of the major embayed ice shelves of the Antarctic continent, draining approximately 14% of the East Antarctic Ice Sheet [Allison, 1979]. However, its shape is considerably different to the other major embayed ice shelves surrounding Antarctica, namely the Filchner-Ronne Ice Shelf and the Ross Ice Shelf (hereafter FRIS and RIS, respectively). The influence of tides on the circulation, induced vertical mixing and melting in the cavities beneath these other major embayed ice shelves have been previously investigated [Robertson *et al.*, 1998; Robertson, 2005; Makinson and Nicholls, 1999; MacAyeal, 1984a, 1984b]. The aims of this study are to carry out a similar investigation on the tidally induced mixing beneath the AIS. The hypothesis is that, like the other ice shelves, the oceanographic conditions in some areas of the AIS cavity are likely to be driven by tidal, rather than purely thermohaline, processes.

[3] Tidal processes are capable of altering the transfer of heat and salt in the ice shelf cavity, and consequently the mean thermohaline circulation. An overturning circulation beneath the AIS has been described by Williams *et al.* [1998a, 1998b]. Under these conditions, the water in contact with the ice shelf base is an outward flowing fresh, cold water mass (Ice Shelf Water, ISW) which isolates the ice shelf base from the relatively warm, saline water mass (Low- or High-Salinity Shelf Water, LSSW and HSSW respectively) which flows into the cavity nearer to the seabed. To initiate melting at the ice shelf base, the warm but dense water must come into contact with the ice. One mechanism previously suggested by MacAyeal [1984b] and Makinson and Nicholls [1999] is via tidal mixing whereby small-scale turbulence is generated at the seabed and ice shelf base by tidal currents. Given the thick ice cover of 300–2500 m, turbulence generation by other means requiring air-sea contact is improbable. Tidal currents are identified as the most energetic process within the RIS cavity [MacAyeal, 1984a], and the same might be expected beneath the AIS. The LSSW found in the region of the AIS cavity is less dense than HSSW found beneath the other major embayed ice shelves. Thus it could be expected that tidal mixing beneath the AIS will more easily destroy the sub-ice shelf stratification and drive stronger melt rates. However, the tidal range beneath the AIS is not as large as beneath other Antarctic ice shelves (i.e., 1–2 m

<sup>1</sup>Institute of Antarctic and Southern Ocean Studies, University of Tasmania, Hobart, Tasmania, Australia.

<sup>2</sup>Now at CSIRO Marine and Atmospheric Research, Hobart, Tasmania, Australia.

<sup>3</sup>Antarctic Climate and Ecosystems Cooperative Research Centre, University of Tasmania, Hobart, Tasmania, Australia.

<sup>4</sup>School of Geography and Environmental Studies, University of Tasmania, Hobart, Tasmania, Australia.

beneath the AIS, and 4–6 m beneath the FRIS and RIS [Padman *et al.*, 2002].

[4] To investigate the contribution of tidal processes to the oceanographic regime in the vicinity of the ice shelf, a nonlinear, high-resolution, barotropic tidal model is applied to the Prydz Bay, AIS cavity region. A major source of error in numerical ocean models, particularly those involving ice shelves, is associated with the assumed topography. Under ice shelves, inaccessibility means that the water column thickness (WCT) in the sub-ice shelf cavity is particularly difficult to measure. Despite progress toward the precise location of the grounding line of the AIS [Fricker *et al.*, 2002], the water column thickness in the deepest parts of the cavity is still largely unknown. This study determined the sensitivity of the tidal response of the AIS system to cavity geometry, thereby determining a best estimate cavity shape based on observed tides in the vicinity of the ice shelf.

## 2. Model Description

[5] Previous modeling studies of the AIS cavity [Williams *et al.*, 1998b, 2001, 2002] used a model geometry defined by Williams *et al.* [1998b]. Since this work, the AIS ice draft and grounding line has been redefined [Fricker *et al.*, 2002], and additional sub-ice shelf topography data has been obtained (A. Ruddell, Antarctic Co-operative Research Centre, unpublished ice draft and bed elevation data for the Amery Ice Shelf, 2001, hereinafter referred to as Ruddell, unpublished data, 2001). The redefined grounding line shows marked inconsistencies with the previously reported position used by Williams *et al.*, extending  $\sim 240$  km further upstream [Fricker *et al.*, 2002]. The more recently collected ice draft and bathymetry data indicate differences of up to 326 m between data and the previously used model geometry. These differences necessitate the generation of a new, and quite different, model geometry for this study.

[6] In order to investigate the interaction between the ice shelf cavity and the open ocean, the region modeled in this study included the AIS cavity and Prydz Bay, extending to the continental shelf slope. The model domain extends from  $73^{\circ} 20'S$  to  $66^{\circ}S$  in latitude, and from  $66^{\circ}E$  to  $78^{\circ}E$  in longitude. The grid spacing is  $1/10^{\circ}$  in longitude, and  $1/30^{\circ}$  in latitude, resulting in a  $120 \times 219$  array.

[7] The world vector shoreline (National Geophysical Data Center, <http://rimmer.ngdc.noaa.gov/coast>) provided a coastline for the nonglacial ice-covered areas. The grounding line of the AIS [Fricker *et al.*, 2002] represents the coastline for the region covered by the floating ice shelf and was also taken as a converging point of the water column thickness: the difference in depth between the ice shelf draft and bed elevation. Although the ice front advances at  $\sim 1300$  m  $yr^{-1}$  [Fricker *et al.*, 2002], the position of the 1998 calving ice front [Fricker *et al.*, 2002] was considered adequate for the application here. Bathymetry in Prydz Bay to the north of the ice front was calculated from a combination of ship track (P. O'Brien, Geoscience Australia, unpublished bathymetry data for the Prydz Bay region, 2001) and BEDMAP [Lythe *et al.*, 2000] data.

[8] Beneath the AIS, measurements of the ice shelf draft and bed elevation were restricted to approximately 70 sparse

locations spread over the ice shelf (Figure 1). Two sets of ice shelf draft measurements have been made at some of these points, with differences of up to 200 m observed (Ruddell, unpublished data, 2001). These 'available data points' are predominantly north of  $71.6^{\circ}S$  and were derived using a range of methods including radio echo sounding and a combination of hydrostatic assumptions and satellite altimetry measurements [e.g., Fricker *et al.*, 2001]. Only 3 points south of this latitude provide measurements of ice shelf draft and none of these provide estimates of bed elevation. Therefore nothing is known of the cavity shape south of  $71.6^{\circ}S$ . BEDMAP ice thickness data [Lythe *et al.*, 2000] indicates the southern most extent of the AIS grounding line is arguably one of the deepest points of bed elevation on the Antarctic continent.

[9] All available sub-ice shelf bed elevation data and Prydz Bay bathymetry data were interpolated onto the model grid using an inverse distance method to provide a smooth map of bed elevation over the entire model domain. Three model grids were created by varying bed elevation in regions away from the available data points. In particular bed elevation was adjusted south of  $71.6^{\circ}S$  so that mean water column thickness over this region was between 50 to 600 m so that sensitivity of the tidal solution to the cavity shape could be determined. North of  $71.6^{\circ}S$ , some variation of bed elevation was allowed in regions of sparse data. Only one ice draft topography was created, as ice draft is the better known of the two variables. Three water column thickness topography grids were then determined from the depth difference between the ice draft and the three bed elevation topography grids. These are (1) the shallow topography (mean WCT within the cavity of 185 m, topography A), (2) the mid-depth topography (mean WCT of 350 m, topography B), and (3) the deep topography (mean WCT of 412 m, topography C). A fourth model topography (called "CADA") was defined; it is similar to the topography used within the CATS00.10 and CADA00.10 series of models [Padman *et al.*, 2002]. This topography consisted of the Williams *et al.* [1998b] cavity geometry interpolated onto a model grid constrained by the grounding line of Fricker *et al.* [2002]. A minimum WCT of 50 m was specified for each model topography, except topography A for which 20 m was specified. Figure 2 displays a longitudinal section of the zonally averaged, bed elevation and ice draft for each of the four model grids. Figure 3 displays a map of the WCT for topography B.

[10] The Model for Estuaries and Coastal Oceans (MECO) model (described by Walker and Waring [1998] and validated by Walker [1999] and Hemer *et al.* [2004]) was used in a two-dimensional barotropic mode to simulate tides in the AIS cavity and Prydz Bay. Consistent with previous barotropic Antarctic sub-ice shelf tidal models [MacAyeal, 1984a; Robertson *et al.*, 1998; Makinson and Nicholls, 1999; Lefevre *et al.*, 2000; Padman *et al.*, 2002], the water depth term,  $H(x, y)$  in the model equations represents water depth in the open ocean, and WCT in the ice shelf cavity.

[11] The seabed stress within the model is related to the depth mean current using a quadratic friction law with a bottom friction coefficient,  $C_D$ , of 0.003, consistent with that used by other models [MacAyeal, 1984a; Robertson *et al.*, 1998; Makinson and Nicholls, 1999; Padman *et al.*,

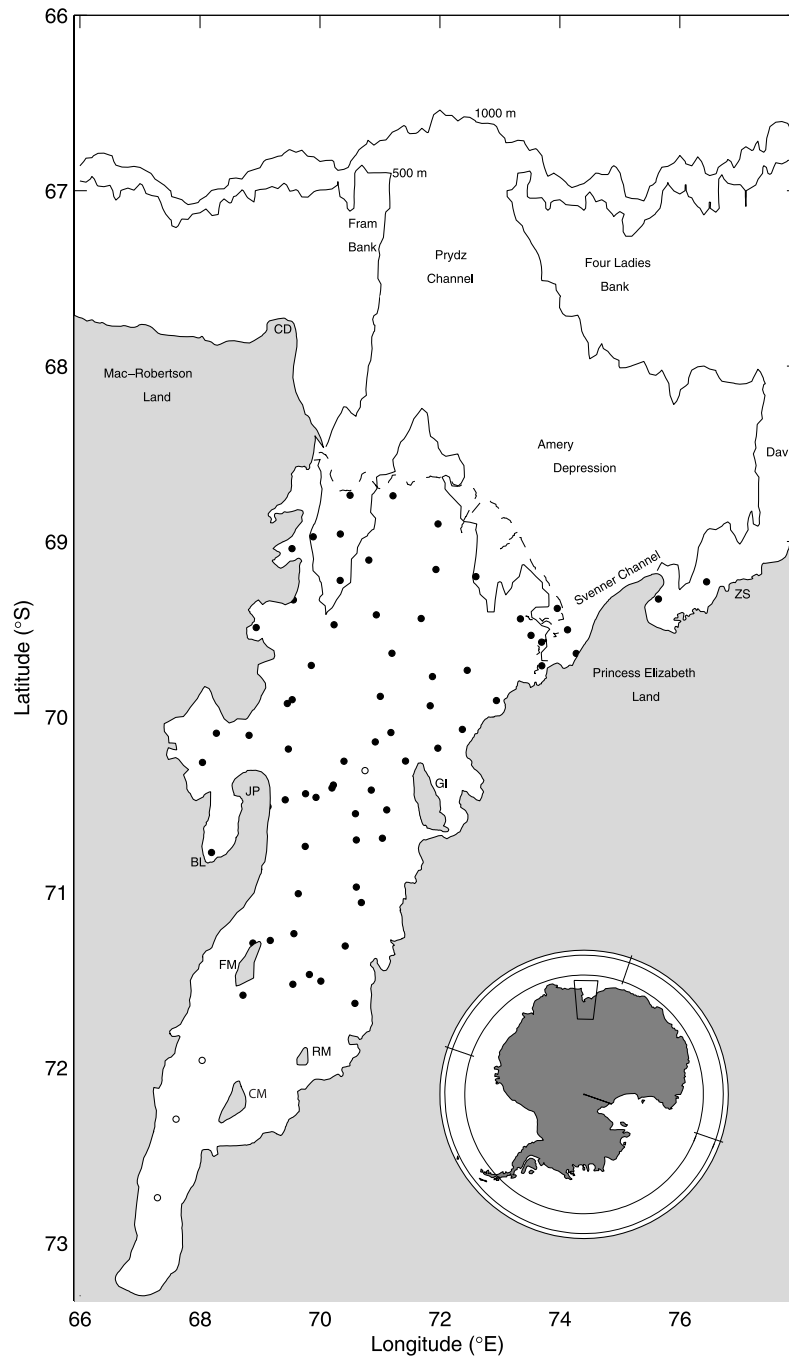


**Figure 1.** Location of bed elevation and ice draft measurement on the Amery Ice Shelf (from A. Ruddell, Antarctic Co-operative Research Centre, unpublished ice-draft and bed elevation data for the Amery Ice Shelf, 2001). Solid circles represent locations where both bed elevation and ice draft measurements are available; open circles represent points where only ice draft measurements are available. The inset shows the location of the Amery Ice Shelf and Prydz Bay in East Antarctica. The locations of Zhong-Shan (ZS), Beaver Lake (BL), Cape Darnley (CD), Jetty Peninsula (JP), Clemence Massif (CM), Robertson Massif (RM), Fisher Massif (FM), and Gillock Island (GI) are also shown.

2002]. Sensitivity studies in which  $C_D$  was varied between 0.0020–0.0035 were carried out, and resulted in only minor variations in simulated tidal height and currents. Beneath the ice shelf area,  $C_D$  was doubled to account for the additional drag at the ice-ocean interface. Apart from

providing a second frictional surface and reducing the water column thickness, the ice shelf had no influence on the tides in this model.

[12] A horizontal viscosity coefficient,  $A_H$ , of  $100 \text{ m}^2 \text{ s}^{-1}$  was specified. The same value was used by *MacAyeal*

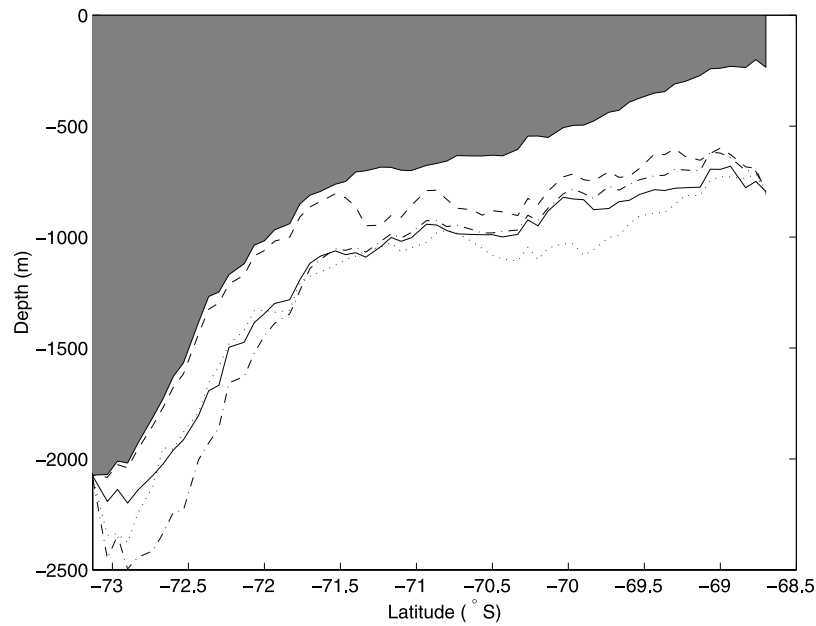


**Figure 2.** Zonally averaged bed elevation for the cavity of the four model topographies presented in this study. Dashed line, topography A; solid line, topography B; dash-dotted line, topography C; dotted line, topography CADA. Filled section represents the zonally averaged ice draft.

[1984a] in the Ross Sea, and by *Makinson and Nicholls* [1999] in the Weddell Sea, and is an order of magnitude smaller than that used by *Robertson et al.* [1998] in the Weddell Sea.

[13] Along the open boundary, time series of sea surface heights for each node were used to force the model. Tide height coefficients obtained from the CADA00.10 model [Padman et al., 2002] were interpolated onto the boundary nodes. The amplitude (h) and phase (g) of 6 tidal constituents ( $Q_1$ ,  $O_1$ ,  $K_1$ ,  $N_2$ ,  $M_2$ ,  $S_2$ ) were used. Within our model domain, the model was forced by the astronomical tide-generating force. An 8-s time step was chosen to satisfy the Courant-Friedrichs-Lewy (CFL) condition.

[14] Initial conditions were of zero current and an undisturbed sea surface. The model was run for 50 days, with the sea surface elevations and currents being recorded hourly over the final 30 days. The MATLAB T\_TIDE software [Pawlowicz et al., 2002] was used to carry out a harmonic analysis of sea surface elevations and currents, yielding amplitude (h) and phase (g) [Pugh, 1987] for the six tidal constituents over the entire grid. The amplitude and phase of the eastward and northward components of each tidal current constituent were then used to construct tidal ellipses.

[15] Dominant sources of error in the model were uncertainties in the bathymetry and boundary conditions and the use of a depth-averaged model. Topographies A, B, C, and CADA were used to assess bathymetric errors and to obtain a best estimate of the cavity shape. The boundary conditions were dependent on the accuracy of the CADA00.10 model, which in the region of Prydz Bay waters, is believed to be quite good due to assimilation of tide gauge data from the nearby Australian Antarctic bases of Davis and Mawson [Padman et al., 2002]. Other potential sources of error are

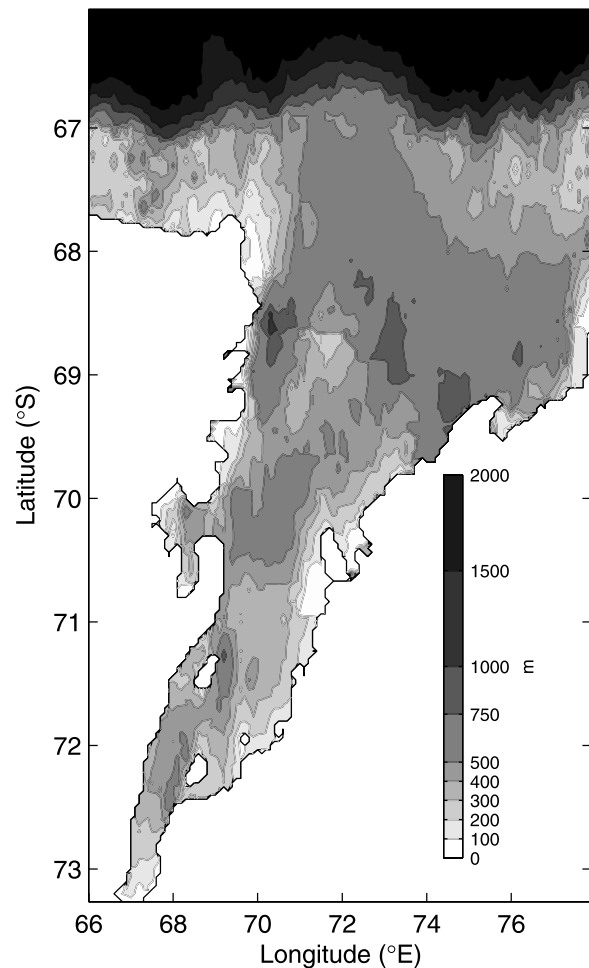


**Figure 3.** Water column thickness (m) for topography B.

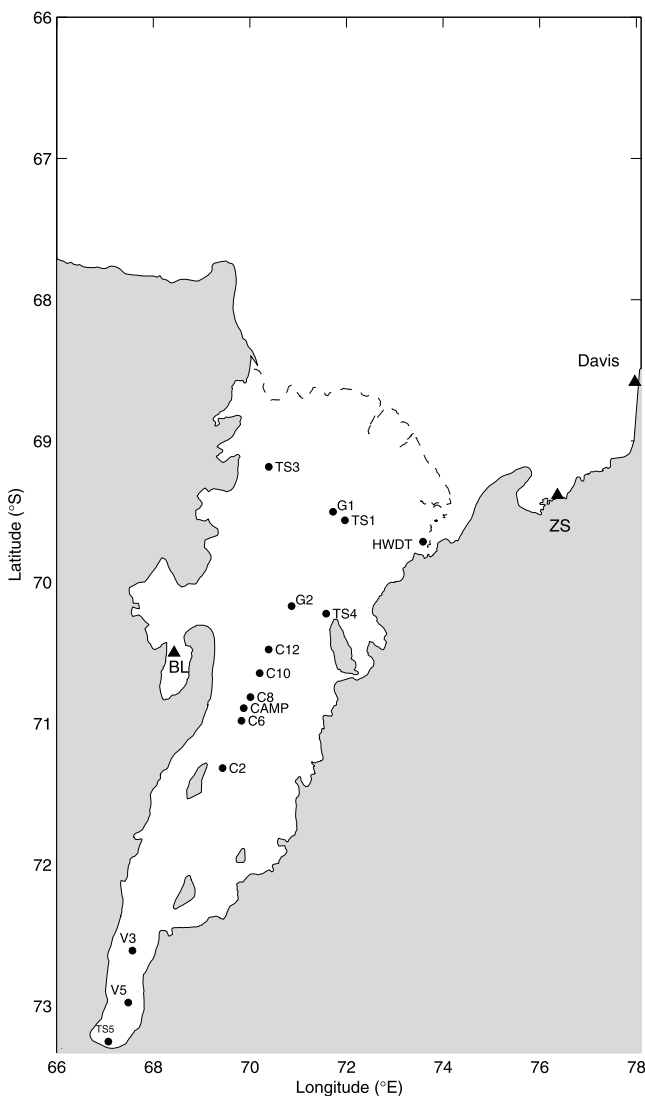


**Figure 4.** Location of tide gauges and GPS sites from which tidal elevation data is available. ZS, BL, and Davis (indicated by triangles) represent the locations of the Zhong-Shan, Beaver Lake, and Davis tide gauges, respectively.

the parameterizations of bottom and lateral shear stresses, the absence of any description of sea ice, and the neglect of baroclinic effects and ice shelf flexure.

### 3. Available Data for Validation

[16] Two types of sea surface elevation measurements were available for model validation and input. Conventional tide gauge data were obtained from Davis, Zhong-Shan and Beaver Lake, while other elevation data were obtained from GPS measurements made on the ice shelf, which was assumed to be freely floating [King *et al.*, 2003]. The data from five GPS sites (Figure 4) have records long enough so that tidal analysis will resolve  $M_2$  from  $S_2$  and  $K_1$  from  $O_1$  (i.e., greater than 15 days). A further ten GPS sites have shorter records, and it should be noted that errors in specific constituents will become

larger as the record lengths become shorter. All available sea level records are summarized in Table 1.

## 4. Water Column Thickness Sensitivity

[17] Model runs were carried out using each of the four topographies, A, B, C, and CADA. The resultant time series and the derived tidal constituents were compared with the available tidal elevation data. In this section, the sensitivity of sea level simulations to changes in the model water column thickness is presented.

### 4.1. Tidal Constituent Comparisons

[18] Tidal amplitude (h) and phase (g) of the four main tidal constituents ( $M_2$ ,  $S_2$ ,  $K_1$  and  $O_1$ ), using topographies A, B, C, and CADA, were compared with the tidal constituents derived from the sea level records. Tidal constituents for the 10 short GPS records were taken directly from King [2002] and also included for comparison.

[19] Table 2 shows the simulated tidal amplitude (h) and phase (g) for each sea level record site, from the model run using topography B. The observed values are shown for comparison. The root mean square of the difference (RMSD) between the simulated and observed tidal amplitudes and phases for each constituent over all sites are also shown. The sensitivity of the model to changes in the water column thickness are summarized in Table 3, which shows the RMSD between the modeled and observed constituents for each run using topography grids A, B, C, and CADA.

[20] The largest amplitude errors are observed toward the southern grounding line of the AIS, where the model shows a greater amplification of semidiurnal tides, and a lesser amplification of the diurnal tides, in comparison to the observations. However, some of this discrepancy may be related to the fact that analyses of short GPS records appear to yield underestimates of semidiurnal amplitudes and overestimates of diurnal amplitudes [King, 2002].

[21] The TS5 site lies within 10 km of the southern extent of the grounding line. Tidal flexure is thought to be important in this zone [MacAyeal, 1984a] and analysis of the TS5 sea level record has therefore been treated separately. Observed constituents at site TS5 indicate strongly reduced amplitudes and large shifts in phase in comparison with values at site V5, for each of the four main constituents. For example, the observed  $M_2$  constituent shows a change in amplitude from 25 cm at V5 (latitude 72.97°S) to 10 cm at TS5 (latitude 73.05°S), and a respective phase change from 238° to 290°. These large changes in tidal constituents, which are not shown in the simulations, are likely to be a result of ice flexure which is neglected in the model.

[22] Diurnal tidal constituents are observed to be the most robust to changes in model bathymetry, showing a slight amplification from ~28 cm at the ice front to ~31 cm at the grounding line for each model run. The RMSD between simulated and observed tidal amplitudes for the diurnal tides is approximately 3–4 cm for all 4 cavity shapes. The phase shift from ice front to grounding line is of the order of 4 degrees for the diurnal tides, and the RMSD between simulated and observed tidal phase from all sites (excluding TS5) is approximately the same for all four cavity shapes (7–8° for  $K_1$ , 11–13° for  $O_1$ ).

**Table 1.** Sites of Observation of Tidal Elevation for the Amery Ice Shelf and Prydz Bay Region<sup>a</sup>

Site	Latitude	Longitude	Record Length, days	Instrument
Davis <sup>b</sup>	68° 35'S	77° 58'E	365+	tide gauge <sup>c</sup>
Zhong-Shan	69° 23'S	76° 22'E	365+	tide gauge
Beaver Lake <sup>d</sup>	70° 48.5'S	68° 9.5'E	39	tide gauge
HWDT <sup>e</sup>	69° 43'S	73° 35'E	26	GPS
TS1	69° 34'S	71° 58'E	48.4	GPS
TS3	69° 11'S	70° 23.5'E	67.8	GPS
TS4	70° 13'S	71° 35'E	64.6	GPS
TS5 <sup>f</sup>	73° 15'S	67° 4'E	82.9	GPS
G1	69° 30'S	71° 43'E	0.83	GPS
G2	70° 10'S	70° 52'E	1.83	GPS
C12	70° 29'S	70° 23'E	1.125	GPS
C10	70° 39'S	70° 12'E	1.2	GPS
C8	70° 49'S	70° 1'E	0.96	GPS
CAMP	70° 53.5'S	69° 52'E	10.5	GPS
C6	70° 59'S	69° 50'E	1.0	GPS
C2	71° 19'S	69° 26'E	1.125	GPS
V3	72° 37'S	67° 34'E	3.5	GPS
V5	72° 59'S	67° 29'E	3.8	GPS

<sup>a</sup>Typical measurement precisions of bottom mounted tide gauges and GPS (vertical motion) are 5–10 mm and 10–50 mm, respectively [King, 2002].

<sup>b</sup>Davis sea level record lies along the eastern open boundary of the model. The data set is used an input data set and therefore not included in the following observation to model comparisons.

<sup>c</sup>Tide gauge data were obtained from the National Tidal Centre, Bureau of Meteorology, Australia.

<sup>d</sup>The longer 1997/1998 Beaver Lake tidal gauge data are used for comparison.

<sup>e</sup>The HWDT GPS was deployed for a period of 31 days. Data gaps in the record reduce the record length to 26 days.

<sup>f</sup>TS5 is not included in the general tidal analysis as it lies within the flexure zone near to the southern grounding line: see text.

[23] Topography A, which is the most shallow, has a mean water column thickness of 185 m. Model results indicate large amplification of the semidiurnal tidal constituents from ~20 cm in open water, to ~115 cm at the southern extent of the cavity. In an open basin, ignoring the effects of rotation and of spatial variation of water column thickness, the natural period of oscillation is given by

$$T_n = 4L / \sqrt{gH}$$

where  $L$  is the length of the cavity ( $510 \times 10^3$  m),  $H$  is the mean WCT (m) and  $g$  is the acceleration due to gravity. A flat bottom basin of 185 m depth has a natural period of oscillation of 13.3 hours, which suggests that resonance of the semidiurnal tides in the prescribed ice shelf cavity is a possibility. The observed tidal amplitudes do not show amplification toward the south of the cavity to the same extent as the simulated values. Some amplification is observed (e.g., the observed (simulated) amplitude of the M<sub>2</sub> tide increases from 20 cm (20 cm) in open water at Zhong-Shan to 25 cm (128 cm) in the south of the cavity at site V5; Table 4). The RMSD between simulated and observed values of amplitude are therefore large (21 and 28 cm for the M<sub>2</sub> and S<sub>2</sub> tides respectively; see Table 3) when using topography A. The simulated phase shift for M<sub>2</sub> and S<sub>2</sub> (from the ice front to the grounding line) of about 65° is also much larger than the observed value of about 25°, suggesting that long tidal waves travel slower in the model cavity than the real cavity, as a result of the water column thickness being too shallow in the south of the domain. There are also large RMSDs in tidal phase of 11° and 31° for the M<sub>2</sub> and S<sub>2</sub> constituents respectively (see Table 3).

[24] Topography B has a mean WCT of 350 m and a slightly shorter natural period of 9.68 hrs. The simulated amplification of the M<sub>2</sub> constituent from 18 cm in open water at Zhong-Shan to 32 cm near the grounding line at

**Table 2.** Comparison of the Simulated and Observed Tidal Amplitude (h) and Phase (g) at 13 Sites in the Model Domain, as Shown in Figure 4, From the Model Using Topography B<sup>a</sup>

Location	M <sub>2</sub>		S <sub>2</sub>		K <sub>1</sub>		O <sub>1</sub>	
	S	O	S	O	S	O	S	O
	<i>Amplitude h, cm</i>							
Zhong- Shan	18	20	17	18	25	27	29	28
Beaver Lake	25	24	24	25	27	28	28	30
HWDT	19	19	19	20	25	26	30	28
TS1	20	21	20	20	25	32	30	28
TS3	20	21	19	16	25	29	30	25
TS4	23	26	23	22	26	32	31	31
G1	20	18	20	16	25	27	30	28
G2	23	24	23	21	26	34	31	35
C12	25	29	25	25	27	31	31	32
C10	25	28	25	24	27	28	32	29
C8	26	27	26	23	27	29	32	30
CAMP	27	26	27	22	27	32	32	33
C6	27	29	27	25	27	39	32	41
C2	29	28	29	25	27	23	32	24
V3	32	23	32	20	28	33	33	34
V5	32	25	33	22	28	34	33	35
RMSD, cm	2.3	2.3	3.2	3.2	4.3	4.3	2.8	2.8
RMSD, %	14	14	22	22	16	16	12	12
	<i>Phase g</i>							
Zhong- Shan	207	212	318	311	281	287	278	259
Beaver Lake	219	253	332	357	286	296	284	288
HWDT	208	215	319	319	282	281	279	272
TS1	213	222	325	323	284	294	281	266
TS3	220	228	333	330	287	296	284	262
TS4	211	211	323	316	283	298	280	259
G1	214	217	327	316	284	305	282	298
G2	214	233	326	332	284	278	282	271
C12	215	228	327	327	285	283	282	276
C10	215	227	328	327	285	289	282	282
C8	216	239	328	339	285	294	282	287
CAMP	216	220	329	320	285	285	283	278
C6	216	230	329	330	285	276	283	269
C2	216	221	329	320	285	275	283	268
V3	216	247	329	347	285	282	283	274
V5	216	238	329	338	285	281	283	274
RMSD	13	13	7	7	7	7	11	11

<sup>a</sup>Tidal phase is in degrees relative to GMT. S, simulated; O, observed.

**Table 3.** Comparison of Observations and Model Results for Each Topography, Showing the RMSD Amplitude (RMSD<sub>A</sub>) and Phase (RMSD<sub>φ</sub>) From the 13 Sea Level Measurement Sites for Each of the Four Main Tidal Constituents<sup>a</sup>

Topography	M <sub>2</sub>		S <sub>2</sub>		K <sub>1</sub>		O <sub>1</sub>	
	RMSD <sub>A</sub> , cm	RMSD <sub>φ</sub> , deg	RMSD <sub>A</sub> , cm	RMSD <sub>φ</sub> , deg	RMSD <sub>A</sub> , cm	RMSD <sub>φ</sub> , deg	RMSD <sub>A</sub> , cm	RMSD <sub>φ</sub> , deg
A	20.9	11	28.0	31	3.6	8	3.2	13
B	2.3	13	3.2	7	4.3	7	2.8	11
C	2.4	13	4.1	7	4.2	7	2.8	11
CADA	3.5	12	2.6	8	3.9	7	2.7	12
CADA00.10	2.6	9	2.4	13	3.0	7	2.5	10
CATS00.10	3.6	8	8.0	8	3.0	7	3.6	10

<sup>a</sup>See Table 1 for sites. The bottom row indicates the comparison of observations and CADA model output.

site V5 more closely matches the observed amplitudes (20 to 25 cm; Table 4). The RMSD in tidal amplitude is less than 5 cm (the instrumental error) for both the M<sub>2</sub> and S<sub>2</sub> tides (2.3 and 3.2 cm respectively; Table 3). The RMSD in phase for the M<sub>2</sub> and S<sub>2</sub> tides are 13° and 7° respectively (Table 3). Of those observations with a reasonable record length, the amplitude and phase errors lie well within the standard errors for each constituent.

[25] Topography C has a mean WCT of 412 m, and a natural period of oscillation of 8.92 hrs. Predicted amplification toward the grounding line is similar to the simulations of topography B (18 to 33 cm for the M<sub>2</sub> constituent; Table 4), although the agreement with observations is slightly worse. However, comparisons are much better than for topography A, the RMSD in amplitude being less than 4.2 cm, and phase differences being the same as for topography B, for all constituents (Table 3).

[26] Topography CADA has a mean WCT of 450 m, and shows similar agreement with observations as grid B. The RMSDs in tidal amplitude are less than 3.9 cm for all constituents, and the RMSDs in phase are approximately the same as those using topographies B or C (Table 3). Topography CADA shows best agreement in amplification toward the grounding line (17 to 27 cm for the M<sub>2</sub> constituent; Table 4), with both the M<sub>2</sub> and S<sub>2</sub> amplitude errors within the instrument error (5 cm) at the V3 and V5 GPS sites. However, the CADA cavity shape does not fit measured WCT values. The RMSD between CADA WCT and measured WCT at the available data points is 220.4 m.

[27] The CADA and CATS models [Padman *et al.*, 2002] provide a solution of the tides beneath the Amery Ice Shelf also at approximately 10km resolution. The RMSD amplitude and phase between the CADA (and CATS) model

solutions and the observations are shown in Table 3. The data-assimilated CADA solution is observed to be of similar accuracy to the forward stepping MECO (topography B) solution. The MECO (topography B) solution indicates a closer agreement to the observations than the forward stepping CATS model. However, the CADA model, as previously indicated, has a topography which is known to be significantly different to more recent measurements, and the final solution is forced via assimilation of several of these “comparison” data sets. On the basis of tidal constituent comparisons, the MECO (topography B) solution provides the best estimate of the barotropic tides beneath the Amery Ice Shelf, using the present best estimate of sub-ice shelf topography.

#### 4.2. Time Series Comparison and Regression Analysis

[28] A regression analysis of modeled and observed time series has been carried out, in addition to time series comparisons at 8 of the sites for which time series data are available. The regression statistics, R<sup>2</sup> and slope, *m*, for each model run are displayed in Table 5.

[29] Time series comparisons at GPS sites HWDT, TS1, TS3, and TS4, and tide gauges Zhong-Shan, and Beaver Lake, depend only weakly on the model run. The model topography in these regions differed little between runs and it appears that variation of water column thickness in the southern portion of the grid has very little influence on sea surface elevations in the northern half of the AIS cavity or Prydz Bay.

[30] However, there are large variations between model runs at GPS sites V3 and V5. The use of topography A results in much lower R<sup>2</sup> values, and much increased RMSDs. As with the comparisons of tidal constituents,

**Table 4.** Observed and Simulated Harmonic Constants (h and g) at Open Ocean Site Zhong-Shan and Southern Cavity Site V5<sup>a</sup>

Location	Grid	M <sub>2</sub>		S <sub>2</sub>		K <sub>1</sub>		O <sub>1</sub>	
		h	g	h	g	h	g	h	g
Zhong-Shan	Observed	0.20	212	0.18	311	0.27	287	0.28	259
Zhong-Shan	A	0.20	208	0.19	322	0.25	281	0.29	277
Zhong-Shan	B	0.18	207	0.17	318	0.25	281	0.29	278
Zhong-Shan	C	0.18	207	0.17	317	0.25	281	0.30	278
Zhong-Shan	CADA	0.17	209	0.16	319	0.26	282	0.29	279
V5	Observed	0.25	238	0.22	338	0.34	281	0.35	274
V5	A	1.28	267	1.55	32	0.36	293	0.39	291
V5	B	0.32	216	0.33	329	0.28	285	0.33	283
V5	C	0.33	216	0.34	328	0.28	285	0.33	283
V5	CADA	0.27	217	0.27	329	0.29	286	0.31	284

<sup>a</sup>The sensitivity of tidal amplification and phase shifts to changes in cavity shape can be observed, particularly with the shallow cavity A. Tidal amplitude (h) is in meters, and tidal phase (g) is in degrees relative to GMT.

**Table 5.** Comparison of Observed and Simulated Sea Level Time Series, Showing the RMSD Between Observed and Simulated Time Series at Points in the Amery Domain for Each Topography Grid<sup>a</sup>

Station	Topography	RMSD	$R^2$	$m$
HWDT (26)	A	0.171	0.783	0.989
HWDT (26)	B	0.162	0.770	1.098
HWDT (26)	C	0.164	0.768	1.083
HWDT (26)	CADA	0.166	0.748	1.167
Zhong-Shan (365+)	A	0.156	0.817	1.163
Zhong-Shan (365+)	B	0.157	0.811	1.207
Zhong-Shan (365+)	C	0.157	0.811	1.203
Zhong-Shan (365+)	CADA	0.166	0.789	1.279
Beaver Lake (39)	A	0.277	0.855	0.709
Beaver Lake (39)	B	0.311	0.468	1.452
Beaver Lake (39)	C	0.315	0.480	1.348
Beaver Lake (39)	CADA	0.292	0.485	1.572
V3 (3.5)	A	0.522	0.405	1.075
V3 (3.5)	B	0.116	0.939	1.096
V3 (3.5)	C	0.112	0.943	1.093
V3 (3.5)	CADA	0.168	0.874	1.230
V5 (3.8)	A	0.734	0.361	0.897
V5 (3.8)	B	0.112	0.952	1.117
V5 (3.8)	C	0.106	0.958	1.111
V5 (3.8)	CADA	0.159	0.909	1.242
TS1 (48.4)	A	0.245	0.689	1.377
TS1 (48.4)	B	0.234	0.719	1.484
TS1 (48.4)	C	0.234	0.718	1.464
TS1 (48.4)	CADA	0.250	0.679	1.608
TS3 (67.8)	A	0.243	0.670	1.429
TS3 (67.8)	B	0.232	0.700	1.460
TS3 (67.8)	C	0.232	0.699	1.441
TS3 (67.8)	CADA	0.242	0.673	1.560
TS4 (64.6)	A	0.258	0.695	1.479
TS4 (64.6)	B	0.225	0.744	1.396
TS4 (64.6)	C	0.225	0.743	1.362
TS4 (64.6)	CADA	0.237	0.721	1.515

<sup>a</sup>RMSD is in m,  $R^2$  is the square of the correlation coefficient, and  $m$  is ratio of observed to simulated elevation. The short GPS data records from V3 and V5 have been included in this analysis as they are useful indicators of the accuracy of the model in the southern part of the cavity. The length (days) of the sea level record at each location is given in parentheses.

there is very little difference between results for the three remaining topographies (B, C, and CADA).

[31] A phase lag is observed at Beaver Lake for all runs. This lag is greatest for Topographies B and C. Local effects not resolved in the model topography are expected to account for this difference.

[32] These comparisons of tidal constituents and sea surface elevation time series show that the best results are obtained with the CADA topography. However, this topography does not agree with available bed elevation measurements (Figure 2) (Ruddell, unpublished data, 2001), the WCT being too large in the northern portion of the AIS, where there are many observations. Topography B is the one which is both consistent with available data and which yields the best tidal simulations. Tidal simulations using topographies B and C are similar, but the deep basin in the south of the topography C is believed to be an overestimate, being 500m deeper than the southern grounding which is possibly the deepest point on the Antarctic continent. The following discussions therefore relate to topography B only.

## 5. Model Results

### 5.1. Tidal Elevations

[33] Tidal observations indicate that the AIS is a region of mixed semidiurnal and diurnal tides, with a range of 1–2 m.

Figure 5 displays elevation amplitude (h) and phase (g) [Pugh, 1987] for the  $M_2$ ,  $S_2$ ,  $K_1$ , and  $O_1$  constituents over the model domain. In the open waters of Prydz Bay, magnitudes of the diurnal tides (0.25 m) are generally observed to be slightly larger than those of the semidiurnal tides (0.15 m). In the ice shelf cavity, amplitudes of semidiurnal constituents are amplified so that at the southern most extent of the grounding line, the amplitude of semidiurnal constituents (0.35 m) is larger than the amplitude of diurnal constituents (0.30 m).

[34] At the southern end of the AIS, the modeled  $M_2$  constituent (Figure 5a) has an amplitude of 0.33m and phase of  $218^\circ$  with respect to Greenwich. At Zhong-Shan, in Prydz Bay, the model indicates an  $M_2$  tidal amplitude of 0.17 m, and phase of  $210^\circ$ . Phase generally propagates from east to west along the Antarctic continent. The phase changes very little beneath the AIS. The  $S_2$  constituent (Figure 5b) behaves in a similar way to the  $M_2$  tide, with similar amplitudes and phase variation beneath the ice shelf. Although no semidiurnal amphidromic points occur in the model domain it is believed that an  $M_2$  amphidrome, just west of the model domain on the Mac-Robertson shelf, strongly influences tides in the region [Padman *et al.*, 2002]. The model cavity exhibits a co-oscillating tidal environment, consistent with a narrow channel, with an

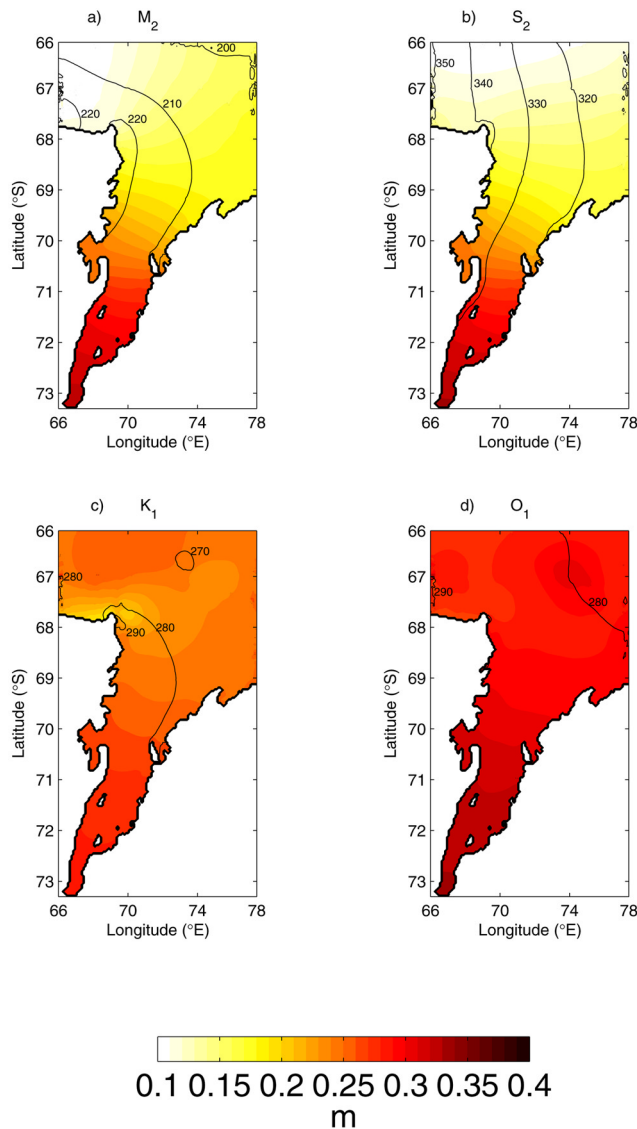


**Figure 5.** Simulated amplitude,  $h$  (m), and phase,  $g$  ( $^\circ$ , GMT), for the (a)  $M_2$ , (b)  $S_2$ , (c)  $K_1$ , and (d)  $O_1$  constituents, with the amplitude shown by color and the phase by the contours. The contour interval is  $10^\circ$  in phase.

increase in amplitude but only small variation of phase and amplitude.

[35] The tidal amplitude for the diurnal constituent,  $K_1$  (Figure 5c), displays only a slight southward increase beneath the AIS. Phase changes for  $K_1$  are small over the entire model domain, but indicate a slight propagation from east to west. The  $O_1$  tide (Figure 5d) behaves similarly to the  $K_1$  tide, with similar amplitudes and phase differences beneath the ice shelf. Four Ladies Bank appears to be a region of complex localized tides. The  $K_1$  constituent decreases in amplitude over the bank while  $O_1$  increases in amplitude. In the shallow water off Cape Darnley the  $K_1$  amplitude is reduced to 0.18 m.

[36] The propagation of tides beneath the AIS differs markedly from beneath the two other major embayed ice shelves around the Antarctic continent, the FRIS and RIS. The width of the AIS is significantly less (about 200 km)

than the widths of the other two ice shelves (about 700 km). This results in a simpler co-oscillation of the tides beneath the AIS, in contrast to the more complex propagating pattern observed beneath the larger ice shelves, associated with clockwise-propagating Kelvin waves [MacAyeal, 1984a; Makinson and Nicholls, 1999]. Near the southern grounding line of the FRIS, the amplitudes of the major semidiurnal and diurnal constituents are around 1 m and 0.4 m, respectively. This leads to a tidal range much greater than that observed beneath the AIS.

## 5.2. Tidal Velocities

[37] The magnitude of the semimajor axis (SMA) of the semidiurnal ellipse is generally less than  $5 \text{ cm s}^{-1}$  beneath the AIS. One region, to the southwest of Gillock Island, indicates semidiurnal SMAs in excess of  $5 \text{ cm s}^{-1}$  for both the  $M_2$  (Figure 6a) and  $S_2$  (Figure 6b) constituents. The semidiurnal SMAs are approximately  $3 \text{ cm s}^{-1}$  beneath the

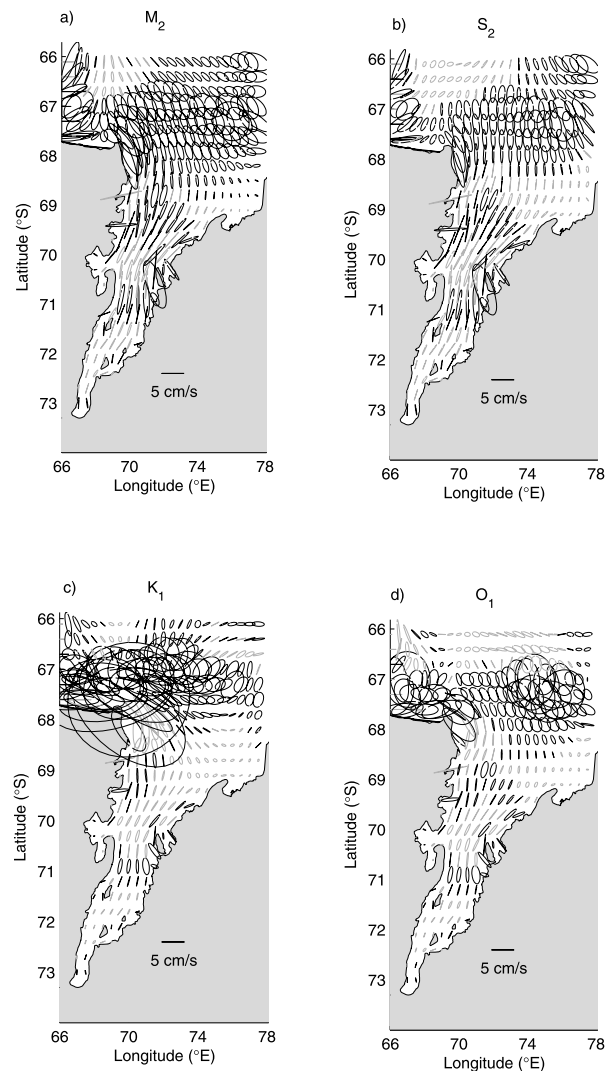


**Figure 6.** Modeled tidal current ellipses at every fifth point in the east direction and every ninth point in the north direction for the (a)  $M_2$ , (b)  $S_2$ , (c)  $K_1$ , and (d)  $O_1$  constituents. Black ellipses indicate counterclockwise rotation; gray ellipses indicate clockwise rotation.

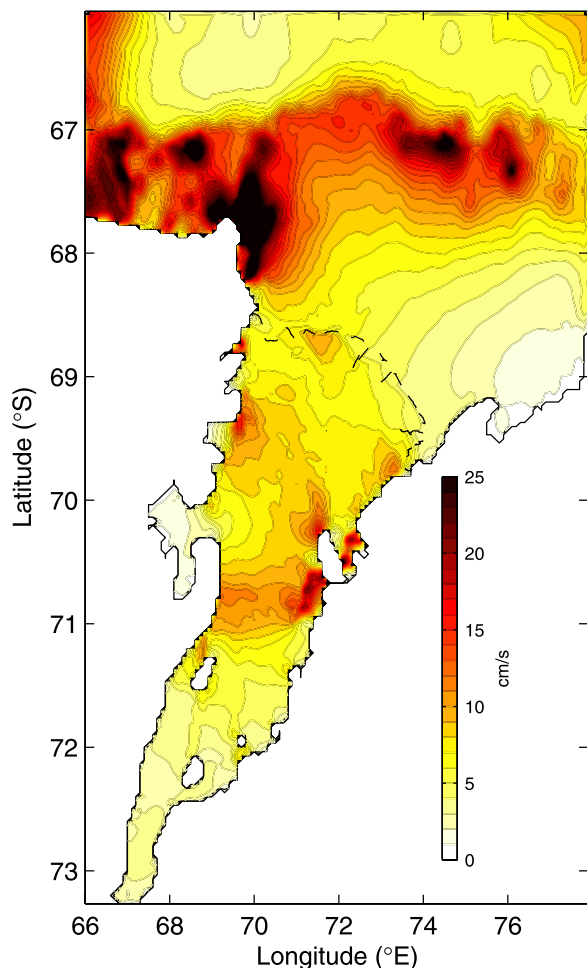


**Figure 7.** Combined typical current speed,  $u_{typ}$  ( $\text{cm s}^{-1}$ ), for the four principal tidal constituents.

northern portion of the AIS and less than  $2 \text{ cm s}^{-1}$  toward the southern grounding line. In the open waters of Prydz Bay, the largest SMAs are located off the point of Cape Darnley, on Fram Bank and on Four Ladies Bank with magnitudes of up to  $10 \text{ cm s}^{-1}$ . Smaller SMAs are observed in regions of deep water, such as Svenner Channel and the Amery Depression. The alignment of the principal axis of the tidal ellipses is approximately north-south throughout the model domain for all constituents. An increase in magnitude of the semidiurnal tidal currents is indicated at the ice front, associated with the reduced WCT in the sub-ice shelf cavity.

[38] Beneath the ice shelf, diurnal currents are weaker than semidiurnal currents; for the diurnal constituents,  $K_1$  (Figure 6c) and  $O_1$  (Figure 6d), SMAs are less than  $2 \text{ cm s}^{-1}$ . However, within Prydz Bay, diurnal currents are larger than semidiurnal currents, with SMAs in excess of  $10 \text{ cm s}^{-1}$  on Fram Bank, off the point of Cape Darnley, and reaching  $7 \text{ cm s}^{-1}$  on Four Ladies Bank. Diurnal currents are small ( $<2 \text{ cm s}^{-1}$ ) in Svenner Channel, and the Amery Depression. Very little amplification of diurnal tidal currents is indicated at the step in water column thickness at the ice front.

[39] A useful measure of typical tidal current magnitude is given by

$$u_{typ} = \sum_{i=1}^4 (u_i^2 + v_i^2)^{1/2}$$

where  $u_i$  and  $v_i$  are the magnitude of the semimajor axis and semiminor axis of the tidal ellipse, with tidal constituent  $i$ , representing the four main tidal constituents (Figure 7).  $u_{typ}$  is roughly the maximum current available as a result of the four tidal constituents. Values of  $u_{typ}$  are typically  $5\text{--}10 \text{ cm s}^{-1}$  beneath the northern portion of the AIS, decreasing to less than  $5 \text{ cm s}^{-1}$  toward the southern grounding line. Small areas surrounding Gillock Island show larger tidal currents of up to  $25 \text{ cm s}^{-1}$ . Only a slight amplification of tidal currents is shown at the large change in WCT at the ice front. Svenner Channel, Prydz Channel, and the Amery Depression show low tidal currents, with  $u_{typ}$  of  $5\text{--}10 \text{ cm s}^{-1}$ . Currents on Fram and Four Ladies Banks are some of the strongest in the model domain, with  $u_{typ}$  of  $30 \text{ cm s}^{-1}$  occurring on Fram Bank.  $u_{typ}$  reaches up to  $52 \text{ cm s}^{-1}$  in the shallower depths off Cape Darnley.

[40] Hemer [2003] presents a comparison of the model tidal velocity predictions to current meter measurements. The observed decrease in tidal currents from the shelf break to the Svenner Channel is qualitatively consistent with descriptions from current meter observations [Nunes Vaz and Lennon, 1996; Hodgkinson et al., 1988, 1991a, 1991b].  $u_{typ}$  values of  $25 \text{ cm s}^{-1}$  on the shelf break are in agreement with the typical tidal velocities of  $25 \text{ cm s}^{-1}$  found by Hodgkinson et al. in this region.

[41] In conclusion, tidal currents beneath the AIS are generally weak, with maximum values of  $u_{typ}$  of  $25 \text{ cm s}^{-1}$  on the eastern side of Gillock Island.  $u_{typ}$  is typically  $5\text{--}10 \text{ cm s}^{-1}$  in the northern portion of the cavity and less than  $5 \text{ cm s}^{-1}$  in the southern portion of the cavity. Tidal currents of up to  $30 \text{ cm s}^{-1}$  occur on the banks on the outer shelf of Prydz Bay, and currents reaching  $52 \text{ cm s}^{-1}$  occur on the inner shelf near Cape Darnley. Tidal currents beneath the AIS are significantly smaller than those beneath the FRIS and RIS, the semimajor axis of the  $K_1$  constituent alone reaching about  $50 \text{ cm s}^{-1}$  in the sub-RIS cavity [MacAyeal, 1984a]. To the west of Berkner Island near the calving ice front of the FRIS, modeled  $u_{typ}$  values under the ice shelf are in excess of  $100 \text{ cm s}^{-1}$  [Robertson et al., 1998]. Residual currents at the front of these other ice shelves are approximately  $6 \text{ cm s}^{-1}$  westward [MacAyeal, 1984a; Makinson and Nicholls, 1999], so the residual tidal currents at the RIS and FRIS ice shelf fronts are of roughly the same magnitude as the maximum tidal currents beneath the AIS. Maximum residual currents across the AIS front, computed from the model presented here, are less than  $1 \text{ cm s}^{-1}$  westward. This small current has little impact on the flux of heat and salt beneath the ice shelf.

## 6. Tidal Energy and Vertical Mixing beneath the Ice Shelf

[42] Within the sub-ice shelf cavity, isolation from atmospheric forcing suggests that tidal currents are likely to be a principal source of energy for mixing [MacAyeal, 1984b;

*Makinson and Nicholls*, 1999]. Frictional drag at the seafloor and at the base of the ice shelf causes vertical shear and turbulence which leads to vertical mixing within the water column. Under a quadratic drag law assumption, the time averaged rate of energy dissipation per unit area,  $D_B$ , is given by

$$D_B = \rho C_D \langle |\bar{u}|^3 \rangle$$

where  $\bar{u}$  denotes the time-variable barotropic velocity, and the angle brackets denote time averaging over the period of tidal analysis. As with the model runs, the drag coefficient,  $C_D$ , is doubled within the cavity to account for friction at the ice shelf base. The mean dissipation rate per unit area due to friction at the ice shelf base and at the seabed, is estimated to be  $0.1 \times 10^{-3} \text{ W m}^{-2}$  for the cavity. Over the  $60,000 \text{ km}^2$  area of the cavity, about 6 MW of energy is therefore dissipated through surface drag. In comparison to the other major embayed ice shelves, *Robertson et al.* [1998] estimated that about 27 GW is dissipated due to friction in the FRIS cavity, at a mean rate of  $67 \times 10^{-3} \text{ W m}^{-2}$ , while *MacAyeal* [1984b] estimated that about 3.5 GW of tidal energy is dissipated due to friction in the RIS cavity, at a mean rate of  $6 \times 10^{-3} \text{ W m}^{-2}$ . Areal dissipation rates beneath the AIS are therefore nearly two orders of magnitude smaller than those beneath the RIS, and nearly three orders of magnitude smaller than those beneath the FRIS, principally due to the smaller tidal current velocities which occur beneath the AIS. The AIS cavity is also a very small total sink of tidal energy around the Antarctic coastline.

[43] These calculations do not consider the energy dissipated beneath the AIS as a result of tidal flexure of the ice. Barotropic models simulating tides beneath the FRIS without including the effect of flexure [*Robertson et al.*, 1998; *Makinson and Nicholls*, 1999] agree well with observations, suggesting that flexure does not dissipate much energy. The AIS tidal model presented here shows greater amplification of the tides toward the south of the cavity than are observed. Ice shelf flexure, which is not included in the model, may account for this behavior. The large difference between model results and observations at site TS5 suggests that ice flexure may be important in the southern AIS cavity, which is relatively narrow (about 60 km wide) compared with the probable extent (about 10 km) of flexure zones (in contrast to the FRIS and RIS which are of much larger extent than the flexure zones). *Smithson et al.* [1996] found that increasing the friction coefficient in a model of the FRIS by a factor of 50 improved the simulations, suggesting that tidal flexure may be an important sink of energy. In this case energy loss by flexure, primarily in a hinge zone at the grounding line, was parameterized by the increase in friction coefficient. Therefore runs of the AIS model were carried out with the friction coefficient beneath the ice shelf increased by factors of 5, 10, 20 and 50, relative to open water values. These changes therefore represented both the inclusion of friction due to the ice/water interface and the increased dissipation as a result of ice shelf flexure near the grounding line. A fiftyfold increase of the friction coefficient decreased tidal elevations in the

southern part of the AIS cavity by only 2 cm, so that the tidal elevation was still overestimated by about 8 cm. Since the AIS has a much longer grounding line, relative to its areal extent, in comparison with other major embayed ice shelves, it is probable that ice flexure is correspondingly more important in terms of energy dissipation. Future tidal models of the AIS should therefore include a better parameterization of tidal flexure than the simple increase of friction coefficient used by *Smithson et al.* [1996].

[44] *MacAyeal* [1984b] and *Makinson and Nicholls* [1999] have estimated the minimum basal melt rate required to maintain stratification in the water column. It is estimated that 1–2% of the tidal energy dissipation is available for vertical mixing of the water column [*Simpson and Hunter*, 1974; *Schumacher et al.*, 1979]. The power,  $P_E$ , required to entrain surface meltwater into an otherwise well mixed water column of salinity  $S$  and depth  $H$ , is given by [*MacAyeal*, 1984b]:

$$P_s = -\Phi \rho \beta g S H / 2$$

where  $\beta = \frac{1}{\rho} \left( \frac{\partial \rho}{\partial S} \right) = 0.8 \times 10^{-3}$ ,  $\rho$  is the water density and  $\Phi$  is the rate of freezing (or melting if  $\Phi < 0$ ). LSSW, of salinity ( $S$ ) about 34.6 occupies the lower part of the AIS cavity, while HSSW ( $S \sim 34.75$ ) is the dominant water mass under the RIS and FRIS [*MacAyeal*, 1984b; *Makinson and Nicholls*, 1999]. The power available from tidal dissipation,  $P_D$ , is:

$$P_D = \alpha \rho C_D \langle |\bar{u}|^3 \rangle$$

where  $\alpha$  is the fraction of total energy available for vertical mixing.  $\alpha$  is here assigned a value of 0.015 for consistency with previous sub-ice shelf models [*MacAyeal*, 1984b, *Makinson and Nicholls*, 1999]. Therefore, for a water column to be well mixed, the rate of negative freezing (i.e., melting) must be less than  $\Phi_M$ , given by [*MacAyeal*, 1984b] as

$$\Phi_M = \frac{\alpha \rho C_D \langle |\bar{u}|^3 \rangle}{\rho \beta g S H / 2}$$

In areas where the rate of negative freeze (melt) is greater than  $\Phi_M$ , stratification will prevail. The spatial distribution of  $\Phi_M$  beneath the AIS indicates no value in excess of  $1 \times 10^{-3} \text{ m yr}^{-1}$ ; the largest value being in the zone of stronger currents to the southwest of Gillock Island. Throughout most of the AIS cavity,  $\Phi_M$  is significantly less than estimated melt rates in the cavity [*Fricke et al.*, 2001; *Williams et al.*, 2002]. Under the assumption that tidal mixing is the predominant mechanism which destroys stratification in the sub-ice shelf cavity (as suggested by *MacAyeal* [1984b] and *Makinson and Nicholls* [1999]), this result suggests a well-stratified environment, weak vertical transfer of heat, and little basal melting. Consequently, another mechanism must provide the heat necessary for melting, the obvious contender being advection in the

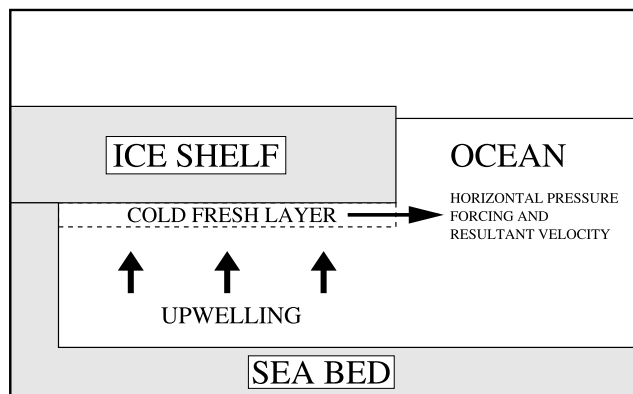


**Figure 8.** Idealized representation of the buoyancy force acting beneath a floating ice shelf. The buoyancy force causes the upwelling of warmer and denser water which comes into contact with the base of the ice shelf, with no requirement for bulk tidal mixing.

baroclinically driven upwelling in the cavity, which is shown schematically in Figure 8. The buoyancy force causes the upwelling of warmer and denser water which comes into contact with the base of the ice shelf, with no requirement for bulk tidal mixing. This circulation is sustained by continued basal melting.

[45] Approaching the grounding line, it is expected a threshold is reached where the tides become sufficiently strong (as the water column thickness decreases, or “pinches” out) to overcome the stratification in the cavity. However, this threshold is not located in this study (which is modeled to a scale where WCT is greater than 50 m), indicating that the influence of barotropic tides in the Amery Ice Shelf cavity are restricted to the complex grounding line zone.

## 7. Conclusions

[46] The application of a barotropic tide model to the AIS cavity has resulted in a number of major conclusions.

[47] 1. The water column thickness of the AIS cavity has been adjusted in order to obtain good agreement between modeled and observed tides. This has been combined with ice draft data to determine the seabed elevation, for which there are no good observations in the deeper parts of the cavity. This new topography (and others derived using this technique) will be used for three-dimensional baroclinic models which are currently under development. In addition, the bathymetric data will be refined through an ongoing program collecting seismic and airborne ice radar data [Tassell, 2004].

[48] 2. The tidal regime of the AIS cavity has been described. The tides are mixed, semidiurnal with a range of 1–2 m. In contrast with the other major embayed Antarctic ice shelves (RIS and FRIS) which display a propagating Kelvin wave, the AIS acts as a narrow channel with the tides co-oscillating along the cavity.

[49] 3. Maximum tidal current speeds within the AIS cavity are shown to be weak. The maximum velocities obtainable for the 4 main tidal constituents in the cavity are  $25 \text{ cm s}^{-1}$ . Throughout most of the cavity, however, maximum tidal current speeds are in the range of  $5\text{--}10 \text{ cm s}^{-1}$ .

Weak tidal residual currents, with velocities of approximately  $1 \text{ cm s}^{-1}$  westward, flow along the ice shelf front. The magnitudes of these residual currents are believed to be small compared with baroclinic currents in the same region.

[50] 4. The AIS cavity is a very small sink of tidal energy, dissipating about 6MW of tidal energy through surface drag at the seabed and ice-ocean interface. This is significantly less than the energy dissipation beneath the other major embayed Antarctic ice shelves. Given the narrowness of the AIS cavity, the effect of ice shelf flexure on tidal energy dissipation should be considered in future models.

[51] 5. Away from the complex grounding line zone, tidal induced mixing in the sub-Amery Ice Shelf cavity is insufficient to overcome the stratification which occurs and the outflowing ISW. We conclude that tidal mixing is not as important as previously thought. Warm but dense water is transported to the base of the ice shelf by buoyancy-driven upwelling, rather than by vertical mixing; this is the main source of heat driving basal melting. These processes are being investigated in more detail using a baroclinic model which is currently under development.

[52] **Acknowledgments.** CSIRO Marine Research, Australia, provided the MECO model. The National Tidal Centre, Bureau of Meteorology, Australia, and Matt King provided tidal data for the study region. Laurie Padman provided geometries and simulations for his CADA and CATS models. Andrew Ruddell supplied unpublished ice thickness and bed elevation data for the AIS cavity. Phil O’Brien, Geoscience Australia, supplied unpublished bathymetry data for Prydz Bay. This research was supported by the Antarctic Co-operative Research Centre, Hobart, Australia, and an Australian Postgraduate Award. The authors are grateful to Christopher Watson, Jason Roberts, and three anonymous reviewers for their useful comments on an earlier version.

## References

- Allison, I. (1979), The mass budget of the Lambert Glacier drainage basin, *Antarctica, J. Glaciol.*, *22*, 223–235.
- Fricker, H. A., S. Popov, I. Allison, and N. W. Young (2001), Distribution of marine ice beneath the Amery Ice Shelf, *Geophys. Res. Lett.*, *28*, 2241–2244.
- Fricker, H. A., I. Allison, M. Craven, G. Hyland, A. Ruddell, N. W. Young, R. Coleman, M. King, K. Krebs, and S. Popov (2002), Redefinition of the grounding zone of the Amery Ice Shelf, East Antarctica, *J. Geophys. Res.*, *107*(B5), 2092, doi:10.1029/2001JB000383.
- Hemer, M. A. (2003), The oceanographic influence of sedimentation on the continental shelf: A numerical comparison between tropical and Antarctic environments, Ph.D. thesis, 355 pp., Univ. of Tasmania, Hobart, Tasmania, Australia.
- Hemer, M. A., P. T. Harris, R. Coleman, and J. Hunter (2004), Sediment mobility due to currents and waves in the Torres Strait-Gulf of Papua region, *Cont. Shelf Res.*, *24*, 2297–2316.
- Hodgkinson, R. P., R. S. Colman, K. R. Kerry, and M. S. Robb (1988), Water currents in Prydz Bay, Antarctica, during 1985, *Aust. Natl. Antarct. Res. Exped. Notes 59*, Aust. Antarct. Div., Kingston, Tasmania, Australia.
- Hodgkinson, R. P., R. S. Colman, M. S. Robb, and R. Williams (1991a), Current meter moorings in the region of Prydz Bay, Antarctica, 1986, *Aust. Natl. Antarct. Res. Exped. Notes 81*, Aust. Antarct. Div., Kingston, Tasmania, Australia.
- Hodgkinson, R. P., R. S. Colman, M. S. Robb, and R. Williams (1991b), Current meter moorings in the region of Prydz Bay, Antarctica, 1987, *Aust. Natl. Antarct. Res. Exped. Notes 82*, Aust. Antarct. Div., Kingston, Tasmania, Australia.
- King, M. A. (2002), The dynamics of the Amery Ice Shelf from a combination of terrestrial and space geodetic data, Ph.D. thesis, 278 pp., Univ. of Tasmania, Hobart, Tasmania, Australia.
- King, M. A., R. Coleman, and L. N. Nguyen (2003), Spurious periodic horizontal signals in sub-daily GPS position estimates, *J. Geod.*, *77*(1–2), 15–21, doi:10.1007/s00190-00002-00308-z.
- Lefevre, F., F. H. Lyard, and C. Le Provost (2000), FES98: A new global tide finite element solution independent of altimetry, *Geophys. Res. Lett.*, *27*, 2717–2721.

- Lythe, M. B., D. G. Vaughan, and the BEDMAP Consortium (2000), BEDMAP—Bed topography of the Antarctic, *BAS Misc.* 9, scale 1:10000,000, Br. Antarct. Surv., Cambridge, U. K.
- MacAyeal, D. R. (1984a), Numerical simulations of the Ross Sea Tides, *J. Geophys. Res.*, 89, 607–615.
- MacAyeal, D. R. (1984b), Thermohaline circulation below the Ross Ice Shelf: A consequence of tidally induced vertical mixing and basal melting, *J. Geophys. Res.*, 89, 597–606.
- Makinson, K., and K. W. Nicholls (1999), Modeling tidal currents beneath the Filchner-Ronne Ice Shelf and on the adjacent continental shelf: Their effect on mixing and transport, *J. Geophys. Res.*, 104, 13,449–13,465.
- Nunes Vaz, R. A., and G. W. Lennon (1996), Physical oceanography of the Prydz Bay region of Antarctic waters, *Deep Sea Res., Part I*, 43, 603–641.
- Padman, L., H. A. Fricker, R. Coleman, S. Howard, and L. Erofeeva (2002), A new tide model for the Antarctic ice shelves and seas, *Ann. Glaciol.*, 34, 247–254.
- Pawlowicz, R., B. Beardsley, and S. Lentz (2002), Classical tidal harmonic analysis including error estimates in MATLAB using T\_TIDE, *Comput. Geosci.*, 28, 929–937.
- Pugh, D. T. (1987), *Tides, Surges and Mean Sea-Level*, John Wiley, Hoboken, N. J.
- Robertson, R. (2005), Baroclinic and barotropic tides in the Ross Sea, *Antarct. Sci.*, 17, 107–120.
- Robertson, R. A. L., L. Padman, and G. D. Egbert (1998), Tides in the Weddell Sea, *Antarct. Res. Ser.*, 75, 341–369.
- Schumacher, J. D., T. H. Kinder, D. J. Pashinski, and R. L. Charnell (1979), A structural front over the continental shelf of the eastern Bering Sea, *J. Phys. Oceanogr.*, 9, 79–87.
- Simpson, J., and J. R. Hunter (1974), Fronts in the Irish Sea, *Nature*, 250, 404–406.
- Smithson, M. J., A. V. Robinson, and R. A. Flather (1996), Ocean tides under the Filchner-Ronne Ice Shelf, Antarctica, *Ann. Glaciol.*, 23, 217–225.
- Tassell, H. (2004), A geophysical investigation into the structure and composition of the Amery Ice Shelf, East Antarctica, honors thesis, Univ. of Tasmania, Hobart, Tasmania, Australia.
- Walker, S. J. (1999), Coupled hydrodynamic and transport models of Port Phillip Bay, a semi-enclosed bay in south-eastern Australia, *Mar. Freshwater Res.*, 50, 469–481.
- Walker, S. J., and J. R. Waring (1998), MECO: Model for estuaries and coastal oceans, *Tech. Rep. OMR-118/120*, CSIRO Mar. Res., Hobart, Tasmania, Australia.
- Williams, M., A. Jenkins, and J. Determann (1998a), Physical controls on ocean circulation beneath ice shelves revealed by numerical models, in *Ocean, Ice, and Atmosphere: Interactions at the Antarctic Continental Margin*, *Antarct. Res. Ser.*, vol. 75, edited by S. S. Jacobs and R. F. Weiss, pp. 285–299, AGU, Washington, D. C.
- Williams, M. J. M., R. C. Warner, and W. F. Budd (1998b), The effects of ocean warming on melting and ocean circulation under the Amery Ice Shelf, East Antarctica, *Ann. Glaciol.*, 27, 75–80.
- Williams, M. J. M., K. Grosfeld, R. C. Warner, R. Gerdes, and J. Determann (2001), Ocean circulation and ice-ocean interaction beneath the Amery Ice Shelf, Antarctica, *J. Geophys. Res.*, 106, 22,383–22,399.
- Williams, M. J. M., R. C. Warner, and W. F. Budd (2002), Sensitivity of the Amery Ice Shelf, Antarctica to changes in the climate of the Southern Ocean, *J. Clim.*, 15, 2740–2757.

---

R. Coleman, School of Geography and Environmental Studies, University of Tasmania, Hobart, TAS 7001, Australia.

J. R. Hunter, Antarctic Climate and Ecosystems Cooperative Research Centre, University of Tasmania, Private Bag 80, Hobart, TAS 7001, Australia.

M. A. Hemer, CSIRO Marine and Atmospheric Research, GPO Box 1538, Hobart, TAS 7001, Australia. (mark.hemer@csiro.au)